Phase diagram of the J_1-J_2 Heisenberg model on the kagome lattice

F. Kolley,[1] S. Depenbrock,[2] I. P. McCulloch,[3] U. Schollwöck,[1] and V. Alba[1]

[1]*Department of Physics and Arnold Sommerfeld Center for Theoretical Physics,*
Ludwig-Maximilians-Universität München, D-80333 München, Germany
[2]*Department of Physics and Astronomy, University of California, Irvine, California 92697, USA*
[3]*Centre for Engineered Quantum Systems, The University of Queensland, Brisbane, QLD 4072, Australia*

We perform an extensive density-matrix renormalization-group study of the ground-state phase diagram of the spin-1/2 J_1-J_2 Heisenberg model on the kagome lattice. We focus on the region of the phase diagram around the kagome Heisenberg antiferromagnet, i.e., at $J_2 = 0$. We investigate the static spin structure factor, the magnetic correlation lengths, and the spin gaps. Our results are consistent with the absence of magnetic order in a narrow region around $J_2 \approx 0$, although strong finite-size effects do not allow us to accurately determine the phase boundaries. This result is in agreement with the presence of an extended spin-liquid region, as it has been proposed recently. Outside the disordered region, we find that for ferromagnetic and antiferromagnetic J_2, the ground state displays signatures of the magnetic order of the $\sqrt{3} \times \sqrt{3}$ and the $q = 0$ type, respectively. Finally, we focus on the structure of the entanglement spectrum (ES) in the $q = 0$ ordered phase. We discuss the importance of the choice of the bipartition on the finite-size structure of the ES.

I. INTRODUCTION

The nature of the ground state of the antiferromagnetic spin-1/2 Heisenberg model on the kagome lattice (KHA) has been debated for a long time. Despite substantial analytical and numerical effort, no agreement has been reached yet in the community. The proposed ground states include several valence bond crystals (VBCs) [1–7], and both gapped and gapless spin liquids [8–25].

However, recent density-matrix renormalization-group (DMRG) simulations [26–28] provided convincing evidence that the ground state of the KHA is a gapped spin liquid with topological entanglement entropy $\gamma = \log(2)$ [29–31]. This is compatible with both a spin liquid of the toric-code or double-semion [32,33] type. Although the former appears naturally in mean-field theories of the KHA [9] and for quantum dimer models on the kagome lattice [34,35] and was therefore favored, recent numerical studies provide indirect evidence that the ground state of the KHA is in a double-semion phase [36–39]. This was motivated by the observation of a chiral spin-liquid phase adjacent to the Z_2 phase [23,36]. Notice, however, that a recent theoretical analysis rules out the double-semion scenario [40].

Moreover, it has been suggested that the spin-liquid behavior survives upon introducing a small antiferromagnetic next-nearest-neighbor interaction [31], i.e., in the J_1-J_2 Heisenberg model (J_1-J_2 KHA). This is in contrast to the $T = 0$ phase diagram of the *classical* version of the model. At $J_2 = 0$, the ground state of the classical J_1-J_2 KHA exhibits an extensive degeneracy [41–47]. This is lifted upon introducing an infinitesimal J_2, and the system develops magnetic order [48]. Precisely, for ferromagnetic J_2, the so-called $\sqrt{3} \times \sqrt{3}$ order emerges, whereas in the antiferromagnetic case, one has the $q = 0$ order. The two ordering patterns are shown schematically in Fig. 1. The magnetic order survives in the quantum model, at least for large enough J_2, as it has been established by exact diagonalization studies [49]. However, the precise phase boundary between the magnetically ordered

phases and the disordered spin-liquid region at $J_2 \approx 0$ has not been determined yet (see Ref. [50] for some interesting results obtained using the functional renormalization-group approach).

In this work, by performing SU(2)-symmetric DMRG calculations, we investigate the ground-state phase diagram of the J_1-J_2 KHA as a function of J_1 and J_2. Here we set $J_1 = 1$, considering both positive and negative J_2. We study the finite-size behavior of the static spin structure factor, the spin-spin correlation length, and the spin gap. For ferromagnetic J_2, we provide numerical evidence that magnetic order of the $\sqrt{3} \times \sqrt{3}$ type survives up to $J_2 \lesssim -0.1$. On the other hand, for antiferromagnetic J_2, signatures of the $q = 0$ state already appear at $J_2 \gtrsim 0.2$. In the narrow region at $-0.1 \lesssim J_2 \lesssim 0.2$, although strong finite-size effects are present, our data are compatible with an extended disordered region, suggestive of a spin-liquid behavior [31]. Finally, we analyze the structure of the entanglement spectrum (ES) [51] in the $q = 0$ ordered phase at large $J_2 \gg 0.2$. Recently, it has been suggested that in the presence of continuous symmetry breaking, the low-lying levels in the ES are reminiscent of the so-called tower of states, which appear in finite-size *energy* spectra [52–54]. This correspondence has been checked numerically in Ref. [54] for the J_1-J_2 KHA at large ferromagnetic J_2, i.e., in the presence of the $\sqrt{3} \times \sqrt{3}$ order, and for the two-dimensional (2D) Bose-Hubbard model in the superfluid phase [53]. Here we investigate how the identification of the correct tower-of-states structure in the ES depends on the choice of the bipartition, in finite-size systems.

The article is organized as follows. Section II introduces the J_1-J_2 Heisenberg model on the kagome lattice and the DMRG method. In particular, we describe in detail the geometry used in the DMRG simulations. In Secs. III and IV, we discuss the numerical results for the static spin structure factor and the spin-spin correlation length. The energy gaps are presented in Sec. V. Finally, in Sec. VII, we investigate the structure of the entanglement spectrum in the $q = 0$ ordered phase.
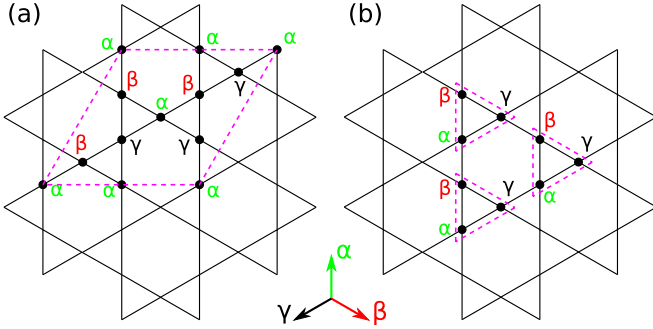
FIG. 1. (Color online) Ordering patterns of the classical J_1-J_2 Heisenberg model on the kagome lattice (J_1-J_2 KHA). The orientations of the spins of the three ferromagnetic sublattices are denoted as α, β, and γ. Spins in different sublattices form an angle of $2\pi/3$. (a) The $\sqrt{3} \times \sqrt{3}$ state arising at $J_2 \ll 0$. (b) The $q = 0$ state, which appears for $J_2 \gg 0$. The dashed lines highlight the unit cells.

II. MODEL AND METHOD

The spin-1/2 J_1-J_2 Heisenberg model on the kagome lattice is defined by the SU(2)-invariant Hamiltonian

$$\mathcal{H} = J_1 \sum_{\langle i,j \rangle} \mathbf{S}_i \cdot \mathbf{S}_j + J_2 \sum_{\langle\langle i,k \rangle\rangle} \mathbf{S}_i \cdot \mathbf{S}_k. \tag{1}$$

Here, $\mathbf{S}_i$ is the spin operator acting on the lattice site i, while $\langle i,j \rangle$ and $\langle\langle i,k \rangle\rangle$ denote nearest- and next-nearest-neighbor sites, respectively. We restrict ourselves to $J_1 = 1$ in (1).

We obtain the ground state of the J_1-J_2 KHA using SU(2)-symmetric DMRG calculations. The geometry used in the simulations is depicted in Fig. 2. The two basis vectors of the kagome lattice are denoted as $\mathbf{e}_1, \mathbf{e}_2$. The unit cell (thicker purple lines) contains three sites. Since DMRG prefers open boundary conditions, we consider kagome cylinders, using periodic (open) boundary conditions in the $\mathbf{e}_2$ ($\mathbf{e}_1$) direction.
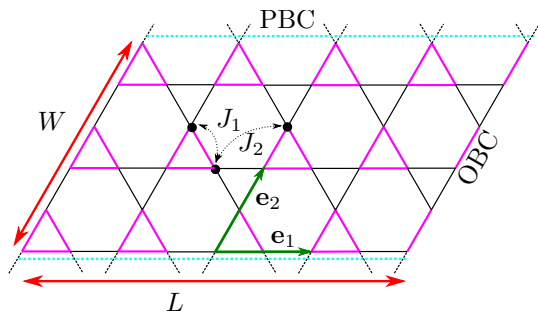

FIG. 2. (Color online) The J_1-J_2 Heisenberg model on kagome cylinders. The spins are located at the vertices of the lattice. The two basis vectors of the lattice are denoted as $\mathbf{e}_1$ and $\mathbf{e}_2$. Periodic (PBCs) and open (OBCs) boundary conditions are imposed along the $\mathbf{e}_2$ and $\mathbf{e}_1$ directions, respectively. The unit cells consist of three sites and are denoted by the thicker (purple) triangles. J_1 and J_2 (see arrows) are the interaction strengths between nearest- and next-nearest-neighbor sites, respectively. The figure shows a cylinder with width $W = 3$ (YC6 geometry) and length $L = 4$. Here, W and L denote the number of unit cells in the $\mathbf{e}_2$ and $\mathbf{e}_1$ directions, respectively. Notice that the unit cells at the right boundary are incomplete in order to alleviate edge effects in the DMRG simulation.

Here we focus on cylinders with width W and length L, where W and L are the numbers of unit cells along the $\mathbf{e}_2$ and $\mathbf{e}_1$ directions, respectively. In order to alleviate spurious effects due to sharp edges, the unit cells at the right boundary of the cylinder contain only two sites. In the Appendix, we show that the results are qualitatively the same for lattices with integer number of unit cells and fully periodic tori. The total number of spins on the lattice used for the main text is given as $W \times (3L + 2)$. Here we consider only cylinders with $W = 3$ and $W = 4$, which, following Ref. [29], are referred to as YC6 and YC8 cylinders. The computational time scales approximate linearly with L and exponentially with W. In our DMRG calculations, we keep up to ~ 5000 SU(2) states, which correspond to approximately 20 000 U(1) states. This allows us to obtain accurate ground-state wave functions for cylinders with lengths $L = 4, 6, 8, 10, 12$ for both the YC6 and YC8 geometries. The largest cylinder considered in this work (with $W = 4$ and $L = 12$) contains 152 spins.

III. STATIC SPIN STRUCTURE FACTOR

Here we discuss the static spin structure factor $S(\mathbf{q})$ obtained from the ground state of the J_1-J_2 Heisenberg model as a function of $-0.2 \leqslant J_2 \leqslant 0.4$. The structure factor is defined as

$$S(\mathbf{q}) = \frac{1}{N} \sum_{i,j=1}^{N} \langle \mathbf{S}_i \cdot \mathbf{S}_j \rangle e^{i\mathbf{q} \cdot (\mathbf{r}_i - \mathbf{r}_j)}. \tag{2}$$

Here, N is the total number of lattice sites, $\langle \cdot \rangle$ denotes the ground-state expectation value, $\mathbf{r}_i$ is the position of site i, and $\mathbf{q}$ is a generic vector in the reciprocal lattice.

Figures 3(a) and 3(b) show the expected structure factors (the circles denote the positions of the peaks in momentum space) for the classical $\sqrt{3} \times \sqrt{3}$ state and the $q = 0$ state, respectively. Figures 3(i)–3(iv) plot the DMRG result for $S(\mathbf{q})$ for $J_2 = -0.2$, $J_2 = 0.0$, $J_2 = 0.1$, and $J_2 = 0.4$. The data are for a YC6 cylinder (with 3×12 unit cells; cf. Fig. 2). Clearly, for $J_2 = -0.2$, sharp peaks with $S(\mathbf{q}_K) \approx 6$ are visible at the K points $\mathbf{q}_K$ of the extended Brillouin zone [see Fig. 3(a), and see Fig. 3(b) for the definition of the high-symmetry points), in agreement with what is expected for the $\sqrt{3} \times \sqrt{3}$ state. Notice that the much smaller peaks at the M points of the first Brillouin zone cannot be resolved with the available system sizes. We observe that at $J_2 = 0$, $S(\mathbf{q})$ is featureless [see Fig. 3(ii)], which signals the absence of magnetic order. On the other hand, already at $J_2 = 0.1$, some peaks start developing at the M points $\mathbf{q}_M$, as expected for the classical $q = 0$ state [cf. Fig. 3(b)]. These become sharper upon increasing J_2 [one has $S(\mathbf{q}_M) \approx 5$ for $J_2 = 0.4$].

All of these features are more quantitatively discussed in Fig. 4, plotting the (squared) antiferromagnetic order parameter $m_{\mathbf{Q}}^2 \equiv S(\mathbf{Q})/N$ versus J_2. Here, $\mathbf{Q}$ denotes the positions of the peaks of the structure factors. Data are for both YC6 and YC8 cylinders [Figs. 4(a) and 4(b)] with lengths $L = 4, 6, 8, 10, 12$. Precisely, Fig. 4 plots $m_{\mathbf{q}_K}^2$ for the $\sqrt{3} \times \sqrt{3}$ order for $J_2 < 0$ (empty symbols) and $m_{\mathbf{q}_M}^2$ (i.e., the order parameter for the $q = 0$ order) for $J_2 \geqslant 0$. In the region $-0.1 < J_2 < 0.2$, $m_{\mathbf{Q}}^2$ is almost featureless and $S(\mathbf{Q})$ itself is nearly size independent. This is compatible with a vanishing
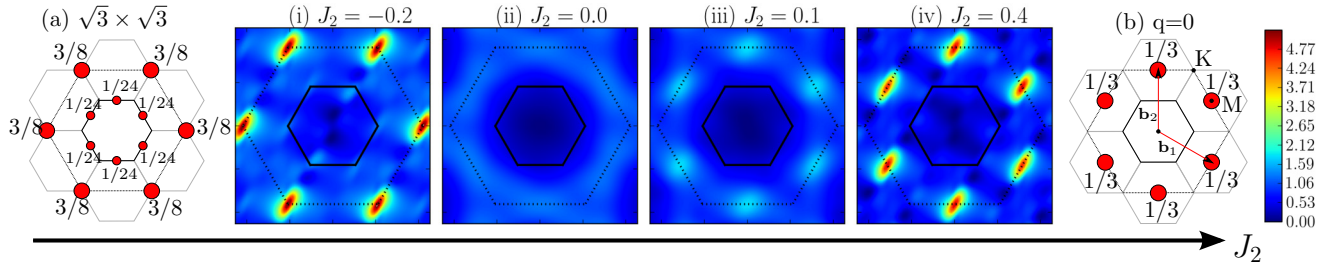
FIG. 3. (Color online) The static spin structure factor $S(\mathbf{q})$ obtained from ground-state DMRG simulations of the J_1-J_2 Heisenberg model on kagome cylinders with 3×12 unit cells (YC6) and several values of J_2: (i) $J_2 = -0.2$, (ii) $J_2 = 0.0$, (iii) $J_2 = 0.1$, (iv) $J_2 = 0.4$. The solid and the dotted lines show the first and the extended Brillouin zones, respectively. (a),(b) The expected structure factors for the *classical* $\sqrt{3} \times \sqrt{3}$ and $q = 0$ states, respectively. In (b), $\mathbf{b}_1$ and $\mathbf{b}_2$ form a basis for the reciprocal lattice, while K and M are the high-symmetry points. The circles denote the peaks in the structure factors, whereas the numbers are the relative peak heights. Clearly, DMRG data at $J_2 = -0.2$ and $J_2 = 0.4$ match the expected structure factors for the $\sqrt{3} \times \sqrt{3}$ and the $q = 0$ states. On the other hand, at $J_2 \approx 0$, the height of the peaks in the structure factor is vanishing [see (ii)], which is compatible with the absence of magnetic order.

order parameter in the thermodynamic limit, as expected in a disordered phase. On the other hand, outside this region, $S(\mathbf{Q})$
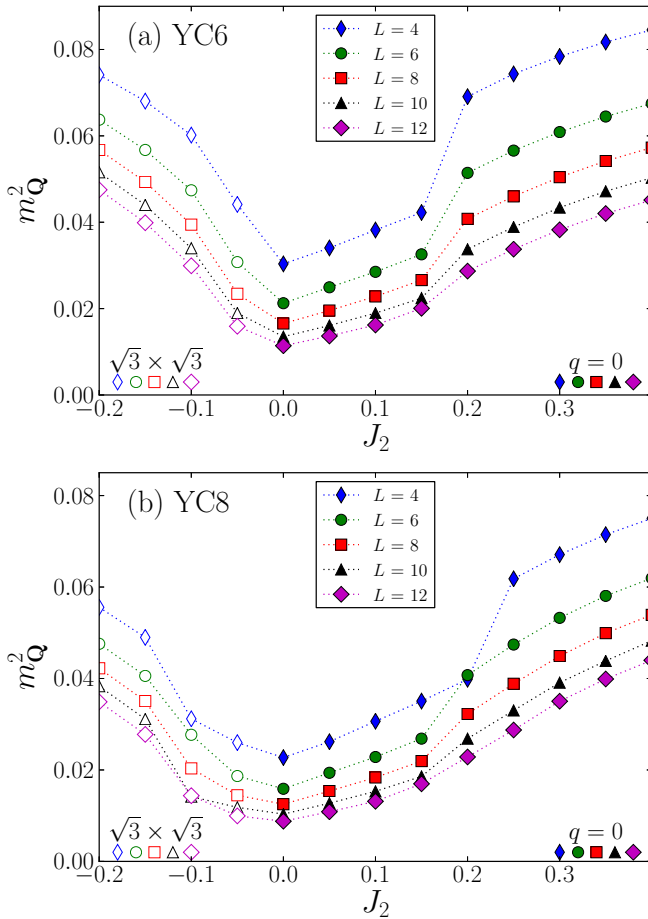

FIG. 4. (Color online) The antiferromagnetic order parameter $m_{\mathbf{Q}}^2 \equiv S(\mathbf{Q})/N$ for the ground state of the J_1-J_2 Heisenberg model plotted as a function of J_2. Here, $\mathbf{Q}$ denotes the position of the peak in the structure factor. (a),(b) The YC6 and YC8 cylinders, respectively. Empty symbols at $J_2 < 0$ are obtained from the peak at the K point in the extended Brillouin zone [corresponding to the $\sqrt{3} \times \sqrt{3}$ state; see Fig. 3(b)], while full symbols at $J_2 \gtrsim 0$ correspond to the M point ($q = 0$ state).

(and, as a consequence, $m_{\mathbf{Q}}^2$) exhibits a stronger dependence on the cylinder size.

A sharp increase of the order parameter can be observed for $J_2 \approx -0.1$ and $J_2 \approx 0.2$, which could signal a phase transition in the thermodynamic limit. Surprisingly, while for $J_2 \gtrsim 0.2$, $m_{\mathbf{Q}}^2$ increases with W, for $J_2 \lesssim -0.1$, it slightly decreases. However, this could be attributed to strong finite-size corrections due to the fact that the YC8 geometry is not commensurate with the large unit cell of the $\sqrt{3} \times \sqrt{3}$ pattern (cf. Fig. 1). We anticipate that this change in the behavior of the order parameter at $J_2 \approx -0.1$ and $J_2 \approx 0.2$ is reflected in the triplet gap (cf. Sec. V). In a magnetically ordered phase, for large system sizes, one should expect $S(\mathbf{Q})/N = m_{\mathbf{Q},\infty}^2 + a/\sqrt{N} + b/N + \cdots$, with $m_{\mathbf{Q},\infty}^2$ the order parameter in the thermodynamic limit. Although a finite-size scaling analysis would allow one to extract $m_{\mathbf{Q},\infty}$, thereby providing conclusive evidence for the presence of magnetic order at $J_2 \ll -0.1$ and $J_2 \gg 0.2$, it would require much larger system sizes than the ones currently available. Finally, from Fig. 4, one should observe that at fixed W, $m_{\mathbf{Q}}^2$ decreases with the cylinder length L, which might signal a vanishing order parameter in the limit $L \to \infty$, as expected, since infinitely long cylinders should exhibit 1D behavior.

IV. SPIN-SPIN CORRELATION LENGTHS

From the structure factor $S(\mathbf{q})$, one can define a correlation length $\xi(\mathbf{Q}, \mathbf{q}_{\min})$ as [55,56]

$$\xi(\mathbf{Q}, \mathbf{q}_{\min}) = \frac{1}{|\mathbf{q}_{\min}|} \sqrt{\frac{S(\mathbf{Q})}{S(\mathbf{Q} + \mathbf{q}_{\min})} - 1}, \qquad (3)$$

where $\mathbf{q}_{\min}$ is the point next to the peak (at $\mathbf{Q}$) of the structure factor. Here we choose $\mathbf{q}_{\min} = \mathbf{b}_1/L$, with $\mathbf{b}_1$ being the reciprocal lattice vector corresponding to the long direction of the cylinder [see Fig. 3(b) for its definition]. Other choices of $\mathbf{q}_{\min}$ are expected to be equivalent in the 2D limit $W, L \to \infty$.

Figure 5 plots $\xi(\mathbf{Q}, \mathbf{q}_{\min})$ for the YC6 [Fig. 5(a)] and YC8 [Fig. 5(b)] cylinders, and various cylinder lengths L. In the figure, we show $\xi(\mathbf{q}_K, \mathbf{q}_{\min})$ (empty symbols) and $\xi(\mathbf{q}_M, \mathbf{q}_{\min})$ (full symbols) in the region with $J_2 < 0$ and $J_2 \geqslant 0$, respectively. The qualitative behavior is the same for
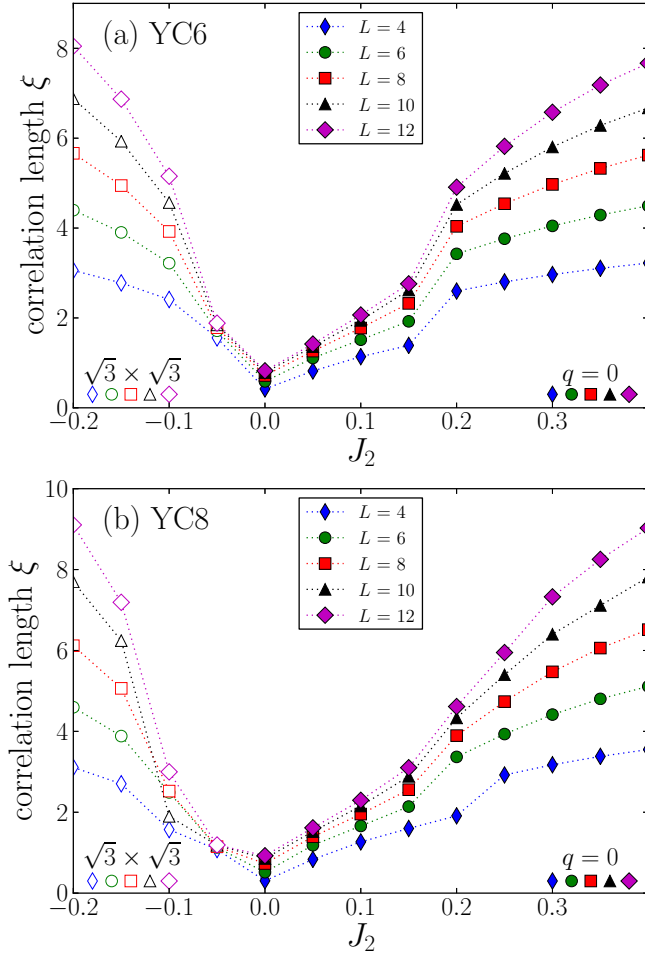
FIG. 5. (Color online) The magnetic correlation length ξ calculated from Eq. (3) as a function of J_2 for (a) the YC6 and (b) the YC8 cylinders at various cylinder lengths L. For $J_2 \leqslant -0.05$, the correlation length (empty symbols) is calculated using $\mathbf{Q} = \mathbf{q}_K$ in (3) and measures the strength of the $\sqrt{3} \times \sqrt{3}$ magnetic order. For $J_2 \geqslant 0$, ξ (full symbols) is defined using $\mathbf{Q} = \mathbf{q}_M$ and it measures the strength of the $q = 0$ magnetic order.

FIG. 6. (Color online) The spin triplet gap Δ_t of the J_1-J_2 Heisenberg model on the kagome lattice as a function of next-nearest-neighbor interaction J_2. Spin gaps for the (a) YC6 and (b) YC8 cylinder, and various cylinder lengths are shown. The gaps are obtained by subtracting the energies of the lowest-energy states in the $S = 0$ and $S = 1$ symmetry sectors, which can be directly accessed by SU(2)-symmetric DMRG simulations.

both YC6 and YC8 cylinders. We obtain small correlation lengths with weak dependence on the cylinder length for $-0.1 \lesssim J_2 \lesssim 0.15$. In particular, at $J_2 = 0$, both correlation lengths are of the order of the lattice constant, as expected in a spin liquid [30]. This behavior reflects that of the order parameter $m_\mathbf{Q}^2$ (cf. Fig. 4). Outside the disordered region, the correlation lengths show an increasing trend as a function of the cylinder length L. For the extremal values $J_2 = -0.2$ and $J_2 = 0.4$ considered in this work, $\xi(\mathbf{Q}, \mathbf{q}_{\min})$ is of the order of the system size.

V. THE SPIN TRIPLET GAPS

Using SU(2)-invariant DMRG simulations, we obtain the lowest-energy eigenstate in both the $S = 0$ and $S = 1$ sectors. We extrapolate their energies in the single-site DMRG truncation error to get the best ground-state energy estimate. Subtracting the extrapolated energies, we obtain the spin triplet gap Δ_t. This is plotted in Fig. 6 for the YC6 and YC8 geometries and several cylinder lengths. Error bars result from
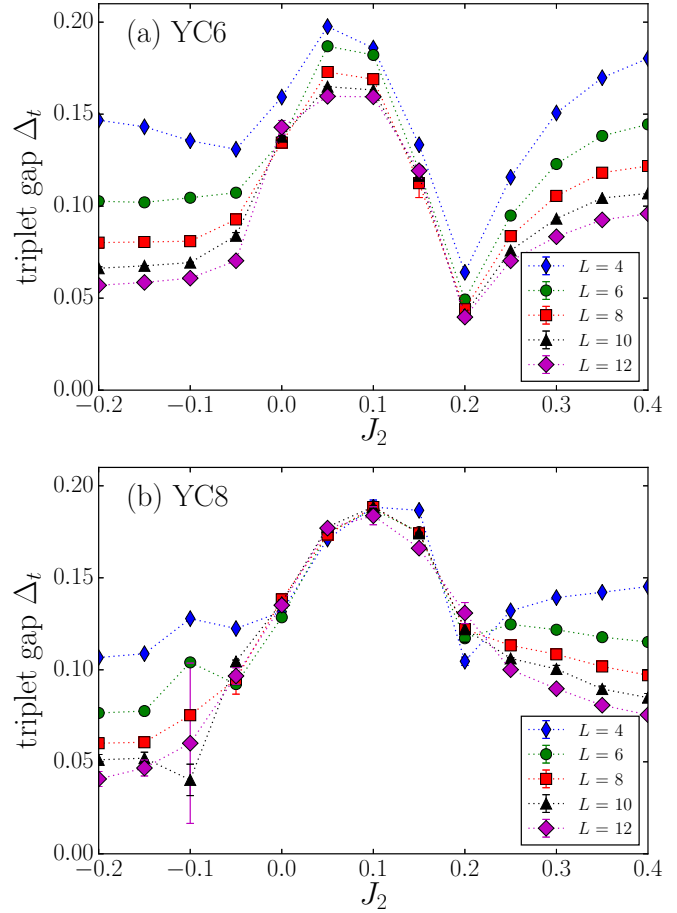
the extrapolation in the truncation error and are, in many cases, smaller than the symbol sizes. In both cases, the gap shows the same qualitative behavior. There is a dome-shaped region for $-0.1 \lesssim J_2 \lesssim 0.2$, with a weak dependence on L and a peak at $J_2 \simeq 0.1$. Remarkably, at the kagome point $J_2 = 0$, the triplet gap is almost independent of the system size, and its value $\Delta_t \approx 0.13$ is in perfect agreement with the result $\Delta_t = 0.13(1)$ of Ref. [30]. A sharp dip is visible at $J_2 \approx 0.2$ and for both geometries, which could suggest a phase transition between the spin-liquid and the $q = 0$ ordered phase in the thermodynamic limit. A less pronounced feature is also visible at $J_2 \approx -0.1$. For both $J_2 \lesssim -0.1$ and $J_2 \gtrsim 0.2$, Δ_t shows a strong dependence on the system size with a decreasing trend as a function of L, W, suggesting a vanishing behavior in the limit $L, W \to \infty$, as expected in a magnetically ordered phase.

It is interesting to investigate the behavior of Δ_t in the limit $L \to \infty$, i.e., for infinitely long cylinders. This is illustrated in Fig. 7, plotting Δ_t as a function of $1/L$ for $J_2 = -0.2, 0.1, 0.4$ and both YC6 and YC8 cylinders. The dotted lines are the linear extrapolations to the infinite cylinder limit. The
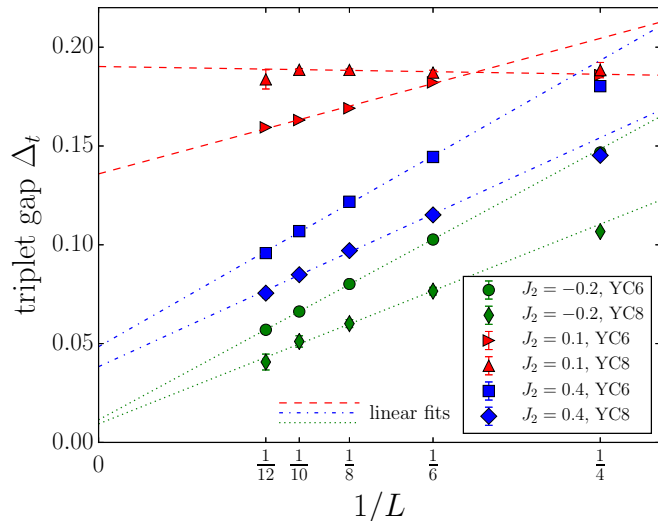
FIG. 7. (Color online) The spin triplet gap in the J_1-J_2 Heisenberg model on the kagome lattice plotted vs $1/L$ for both YC6 and YC8 cylinders. Data for $L = 4,6,8,10,12$ and $J_2 = -0.2,0.1,0.4$ are shown in the figure. The lines denote the linear extrapolations to the infinite cylinder limit.

extrapolated gaps are shown in Fig. 8. The triplet gap shows a peak at $J_2 \simeq 0.1$ with a value of approximately $\Delta_t \approx 0.14$ for the YC6 and $\Delta_t \approx 0.18$ for the YC8 cylinder. It is interesting to observe that the maximum of the gap is not at $J_2 \approx 0$, where the structure factor is featureless (cf. Fig. 4). For larger $|J_2|$, the extrapolated gap exhibits decreasing behavior as a function of J_2. We should remark that although the extrapolated gaps seem to vanish outside the disordered region, this should not be associated with the presence of Goldstone modes, as infinite long cylinders are expected to exhibit 1D behavior and no symmetry breaking.
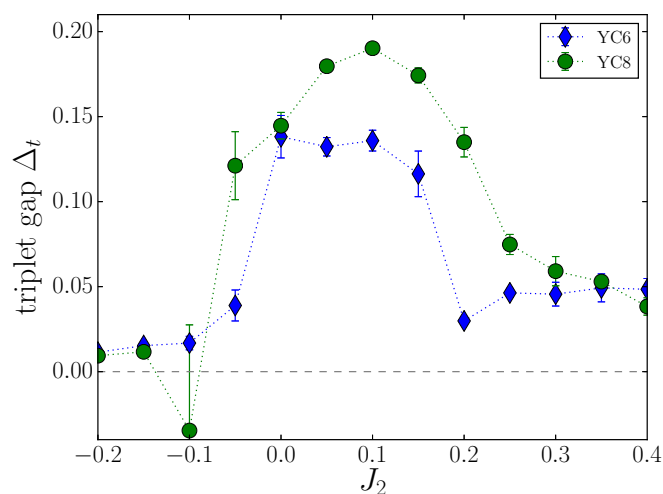

FIG. 8. (Color online) The spin triplet gap Δ_t in the J_1-J_2 Heisenberg model: Extrapolations to the infinitely long cylinder limit. We show Δ_t for both the YC6 and the YC8 cylinders as a function of the next-nearest-neighbor coupling J_2. Error bars result from the extrapolation in the cylinder length (see Fig. 7).

VI. DISCUSSION

Here we discuss the physical implications of the numerical results presented in Secs. III–V. We divide the discussion into three parts for different parameter ranges. First we consider the case $J_2 \lesssim -0.1$, then $-0.1 \lesssim J_2 \lesssim 0.2$, and finally $J_2 \gtrsim 0.2$.

(a) $J_2 \lesssim -0.1$. The static spin structure factor at $J_2 \approx -0.2$ [see Fig. 3(i)] exhibits sharp peaks at the K points of the extended Brillouin zone. The peak positions are in agreement with what is expected for the classical $\sqrt{3} \times \sqrt{3}$ order. Moreover, the DMRG data suggest a sudden increase of the antiferromagnetic order parameter $m_{\mathbf{Q}}^2$ with increasing $|J_2|$. The corresponding spin-spin correlation length is of the order of the system size, and it increases upon increasing $|J_2|$. This could suggest magnetic order of the $\sqrt{3} \times \sqrt{3}$ type in the thermodynamic limit. This is also weakly confirmed by the behavior of the triplet gap Δ_t. We numerically observe that Δ_t decreases upon increasing L and W for $J_2 \lesssim -0.1$, which is consistent with a vanishing behavior in the 2D limit (cf. Figs. 6 and 8), as expected in a magnetically ordered phase, due to the presence of the Goldstone modes.

(b) $-0.1 \lesssim J_2 \lesssim 0.2$. In this region, we observe a dome-shaped triplet gap. For both the YC6 and YC8 geometries, the DMRG data support a finite gap in the infinite cylinder limit (see Fig. 8), excluding the presence of magnetic order. Interestingly, for the YC8 cylinders, this gap is almost independent of the cylinder length. The structure factor is almost featureless (cf. Fig. 3), although some peaks at the M points of the extended Brillouin zone are visible, signalling the onset of the $q = 0$ order at larger J_2. The spin-spin correlation lengths for both the $\sqrt{3} \times \sqrt{3}$ and $q = 0$ magnetic order are of the order of the lattice constant. These results confirm earlier DMRG studies performed at $J_2 = 0$ [29,30], in agreement with an extended Z_2 spin-liquid region around $J_2 = 0$. Notice that our data does not support an algebraic U(1) spin liquid, which would imply a vanishing spin gap, in contrast with what has been found recently by variational Monte Carlo methods [7]. Also, from the present data, we cannot exclude a transition from the Z_2 spin liquid to a valence bond crystal (VBC) for small ferromagnetic J_2, as it was reported in Ref. [7]. Notice that the breaking of the lattice symmetry is hard to detect [57] using the cylinder geometry. In order to detect the VBC phase, it would be useful to study the dimer-dimer correlation function $\langle D_i^\alpha D_j^\beta \rangle$, where $D_i^\alpha \equiv S_{\mathbf{r}_i} \cdot S_{\mathbf{r}_i + \alpha}$, with $\alpha = \hat{x}, \hat{y}$, and the corresponding structure factor $S_d^{\alpha,\beta}(\mathbf{q}) \equiv 1/N \sum_{i,j} e^{i\mathbf{q}(\mathbf{r}_i - \mathbf{r}_j)} \langle D_i^\alpha D_j^\beta \rangle$. Moreover, it would be interesting to calculate the topological entanglement entropy γ, which is expected to be zero in the VBC phase, while it is $\gamma = \log(2)$ in the Z_2 spin-liquid phase. However, this would require larger cylinders in order to perform a precise finite-size scaling analysis of the von Neumann entropy.

(c) $0.2 \lesssim J_2$. We find sharp peaks in the static spin structure factor [cf. Fig. 3(iv)] at the M points of the extended Brillouin zone. This is in agreement with what is expected for the $q = 0$ magnetic order. The triplet gap exhibits a decreasing behavior upon increasing W and L. Correspondingly, the spin-spin correlation length rapidly increases with J_2 (cf. Fig. 5).

VII. ENTANGLEMENT SPECTROSCOPY IN THE $Q = 0$ PHASE

Given a spatial bipartition of the cylinder in parts A and B, the so-called entanglement spectrum (ES) levels [51] $\{\xi_i\}$ are constructed from the Schmidt decomposition of the ground-state wave function $|\psi\rangle$ as

$$|\psi\rangle = \sum_i e^{\xi_i/2} |\psi_i^A\rangle \otimes |\psi_i^B\rangle, \tag{4}$$

where $|\psi^{A(B)}\rangle$ form an orthonormal basis set for subsystem $A(B)$. Alternatively, the ES can be thought of as the spectrum of an effective entanglement Hamiltonian $\mathcal{H}_E$ that is defined as

$$\mathcal{H}_E \equiv \exp(-\rho_A), \tag{5}$$

where ρ_A is the reduced density matrix of subsystem A. Since the DMRG algorithm works directly in the Schmidt basis, the ES is available essentially for free during a ground-state simulation and provides another useful tool to characterize the properties of the ground state.

It has been proposed recently [52] that in a model that breaks a continuous symmetry in the thermodynamic limit, the low-lying part of the ground-state entanglement spectrum (ES) exhibits the tower-of-states structure, which describes the finite-size energy spectrum of the model. In particular, for a spin model that fully breaks the SU(2) symmetry, many features of the low-lying ES levels can be understood in terms of the entanglement Hamiltonian

$$\mathcal{H}_E \propto \frac{\mathbf{S}_A^2}{W} + \cdots, \tag{6}$$

where $\mathbf{S}_A$ is the total spin in subsystem A, and $W \sim \sqrt{N}$ is the cylinder width (cf. Fig. 2). The low-lying spectrum of (6) is shown schematically in Fig. 9, plotting ES levels versus $S_A(S_A + 1)$. In each sector with fixed S_A, there are $(2S_A + 1)^2$ levels (rhombi in the figure) forming the tower of states, which are divided from higher-lying levels by an entanglement gap. The tower-of-states levels exhibit linear behavior with respect to $S_A(S_A + 1)$. Notice that although (6) gives $(2S_A + 1)^2$ degenerate levels in each spin sector, this degeneracy is, in general, lifted, as shown in Fig. 9. The correspondence between the ES and tower of states has been numerically verified in the J_1-J_2 KHA in Ref. [54] for $J_2 = -1.0$, i.e., deep in the $\sqrt{3} \times \sqrt{3}$ ordered phase.

Notice that both the $\sqrt{3} \times \sqrt{3}$ and the $q = 0$ ordering patterns correspond to full breaking of the SU(2) symmetry (see Fig. 1), as they contain three ferromagnetic sublattices. As a consequence, deep in the $q = 0$ phase, one should expect the same tower-of-states structure shown in Fig. 9 in the ES. However, here we provide numerical evidence that the identification of the correct tower of states depends on the choice of the bipartition, at least for small system sizes.

This is illustrated in Fig. 10, plotting the half-system ES for a kagome cylinder with 4×12 unit cells (YC8 geometry) at $J_2 = 1.0$ and for two different bipartitions. The bipartitions are shown in Figs. 10(a) and 10(b): The three ferromagnetic sublattices forming the $q = 0$ state (cf. Fig. 2) are denoted as A, B, C; bonds connecting spins on different sublattices are shown with different colors. While Fig. 10(a) corresponds to
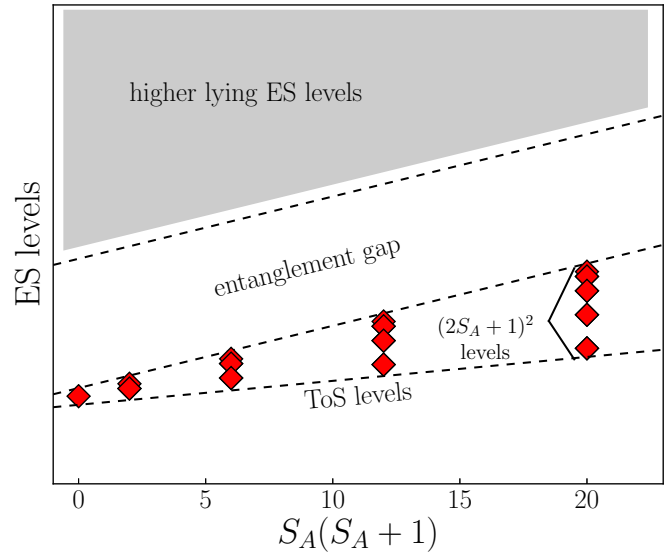

FIG. 9. (Color online) The expected structure of the entanglement spectrum (ES) in the $q = 0$ magnetically ordered phase in the J_1-J_2 Heisenberg model on the kagome lattice. ES levels are plotted vs $S_A(S_A + 1)$, with S_A being the total spin in subsystem A. The rhombi denote the ES levels displaying the tower-of-states structure. The number of tower-of-states levels in each sector with fixed S_A is given as $(2S_A + 1)^2$. These are divided from the higher-lying levels by an entanglement "gap."

a straight cut, Fig. 10(b) has a zigzag structure. One should observe that the straight cut crosses only B-C and A-B bonds, whereas all three types of bonds (A-B, B-C, and A-C) are crossed by the zigzag cut in Fig. 10(b). This suggests that the straight cut might not capture the quantum correlations between sublattices A and C. Notice that for the $\sqrt{3} \times \sqrt{3}$ state, this is not the case as the straight cut would cross all three different types of bonds. The difference between the two cuts is reflected in the corresponding entanglement spectra.

The ES obtained using the straight cut [Fig. 10(a)] is reported in Fig. 10(c). The ES levels are plotted versus $S_A(S_A + 1)$. Full symbols denote the lowest $(2S_A + 1)^2$ levels in each spin sector. Strong deviations from the expected picture in Fig. 9 are visible. In particular, no gap between the tower-of-states levels and the rest of the spectrum is visible. Better agreement with Fig. 9 is found using the zigzag cut, as is clear from Fig. 10(d). For instance, the low-lying levels now show a clear linear behavior with respect to $S_A(S_A + 1)$. Moreover, in the $S_A = 0$ and $S_A = 1$ sectors, the tower-of-states levels are well separated from higher-lying levels by an entanglement gap, although this becomes smaller for $S_A = 2$, when the low-lying levels start mixing with the rest of the spectrum. Finally, we should mention that despite the numerical evidence in Fig. 10, within the available system sizes, we cannot exclude that the difference between the ES in Figs. 10(c) and 10(d) disappears considering larger cylinders.

VIII. CONCLUSION

We performed an extensive DMRG study of the ground-state phase diagram of the J_1-J_2 Heisenberg model on kagome cylinders. We restricted ourselves to $J_1 = 1$, considering both
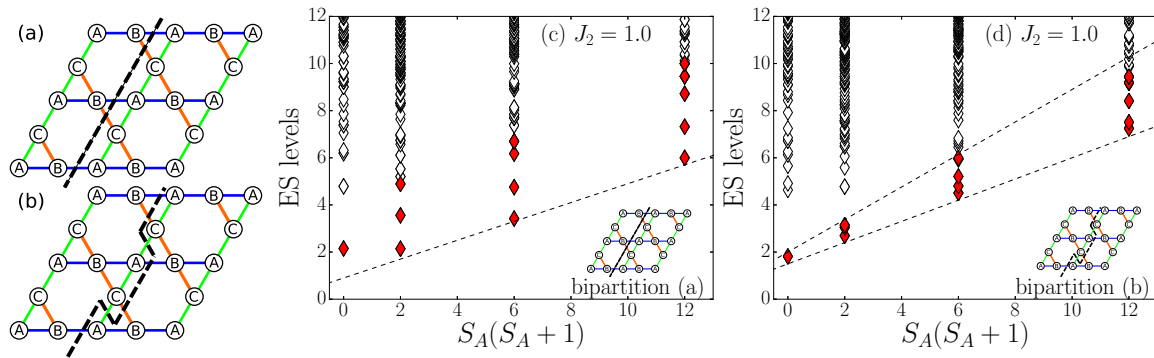
FIG. 10. (Color online) Spin-resolved entanglement spectra obtained from the ground-state wave function of the J_1-J_2 Heisenberg model on the kagome lattice at $J_2 = 1.0$. Data are for a cylinder with 4×12 unit cells. (a),(b) Schematic representation of the $q = 0$ state on the kagome lattice. A, B, and C denote the three ferromagnetic sublattices. Bonds connecting spins in different sublattices are shown with different colors. The black dashed line marks the cut defining the bipartition used to calculate the entanglement spectrum. Two possible cuts are shown: (a) The cut crosses only A-B and B-C bonds, (b) the cut crosses A-B, B-C, and A-C bonds. (c),(d) The entanglement spectra obtained from the bipartitions shown in (a) and (b), plotted vs $S_A(S_A + 1)$, with S_A being the total spin in subsystem A. Each symbol corresponds to a $2S_A + 1$ degenerate multiplet of levels. The red symbols denote the lowest $(2S_A + 1)^2$ levels. Notice that deviations from the expected tower-of-states structure (cf. Fig. 9) are large using the bipartition shown in (a).

antiferromagnetic and ferromagnetic J_2. In particular, we investigated the behavior of the model around the pure kagome point at $J_2 = 0$. To this purpose, we monitored the behavior of the spin triplet gap, the static structure factor, and the magnetic correlation length, as a function of J_2. We should remark that our results are based on finite-size cylinders. Strong finite-size effects do not allow us to provide conclusive results about the phase diagram of the model in the thermodynamic limit.

By comparing the finite-size behaviors of the spin gap, the structure factor, and the correlation lengths, we found numerical evidence suggesting that the ground state of the model displays magnetic order for $J_2 \lesssim -0.1$ and $J_2 \gtrsim 0.2$. Precisely, for $J_2 \lesssim -0.1$, the structure factor exhibits sharp peaks at the K points of the extended Brillouin zone, in agreement with what is expected for the classical $\sqrt{3} \times \sqrt{3}$ state, whereas at $J_2 \gtrsim 0.2$, one observes peaks at the M points, which signal the $q = 0$ magnetic pattern. In both cases, the correlation lengths associated with the two structures show a rapid increase upon increasing $|J_2|$ and the system size. Correspondingly, the triplet gap decreases, suggesting a vanishing gap in the thermodynamic limit. Within the system sizes accessible to the simulations, our results are consistent with the presence of a magnetically disordered phase for $-0.1 \lesssim J_2 \lesssim 0.2$, which is compatible with spin-liquid behavior [31]. In this region, the spin gap shows a weaker dependence on the cylinder size. Moreover, the DMRG data support a finite gap for infinitely long cylinders. The static structure factor is featureless at the $J_2 = 0$ point, and it exhibits not very pronounced structures in the whole region $-0.1 \lesssim J_2 \lesssim 0.2$. The magnetic correlation lengths associated with the $\sqrt{3} \times \sqrt{3}$ and the $q = 0$ order are of the order of the lattice unit.

As a final point, we investigated the structure of the ground-state entanglement spectrum (ES) in the $q = 0$ ordered phase. We found that the identification of the tower-of-states structure, which is associated with the SU(2) symmetry breaking in the thermodynamic limit, depends dramatically on the choice of the spatial bipartition of the state, at least for small system sizes.

Recently, we became aware of two related works. In Ref. [58], a DMRG study of the phase diagram of the J_1-J_2-J_3 Heisenberg model on the kagome lattice is performed, and in Ref. [59], the phase diagram of the J_1-J_2 Heisenberg model on the kagome lattice is studied with a variational Monte Carlo method. The results of both works are in qualitative agreement with the ones reported in this paper.
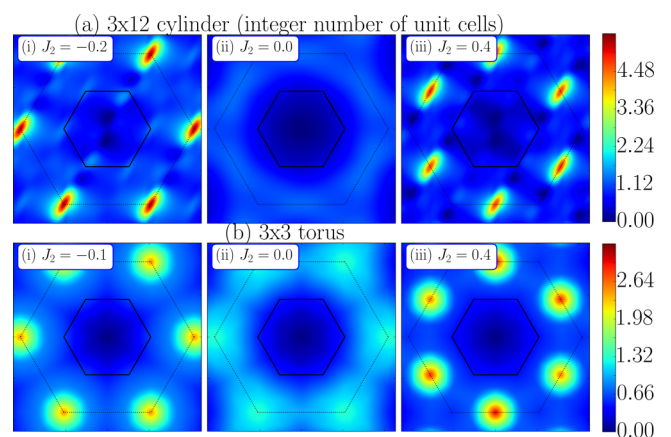
FIG. 11. (Color online) The static spin structure factor $S(\mathbf{q})$ obtained from ground-state DMRG simulations of the J_1-J_2 Heisenberg model (a) on kagome cylinders with integer number of 3×12 unit cells and (b) on small tori with 3×3 unit cells for different values of J_2. The solid and the dotted lines show the first and the extended Brillouin zones, respectively. The spin correlations are qualitatively the same as in Fig. 3 for all J_2 values and boundary conditions.

the Australian Research Council Centre of Excellence for Engineered Quantum Systems, Grant No. CE110001013.

APPENDIX: INDEPENDENCE ON BOUNDARY CONDITIONS

In this work, we used a lattice geometry with a noninteger number of unit cells (cf. Fig. 2). Here we show that this does not affect the phase diagram presented in Fig. 3. We also investigate the effect of boundary conditions, discussing the structure factor for the J_1-J_2 Heisenberg model on kagome tori. In Fig. 11, we present the static spin structure factors for lattices with an integer number of unit cells at $J_2 = -0.2, 0.0, 0.4$, as well as for fully periodic small tori at $J_2 = -0.1, 0.0, 0.4$. For all of the lattice geometries, we find antiferromagnetic correlations corresponding to the $\sqrt{3} \times \sqrt{3}$ state at $J_2 = -0.2$ and $J_2 = -0.1$, and antiferromagnetic correlations corresponding to the $q = 0$ state at $J_2 = 0.4$. At $J_2 = 0.0$, the structure factor for the cylinder geometry with integer number of unit cells is structureless, while for the small torus, the structure factor shows slightly enhanced correlations at the K points of the extended Brillouin zone.

[1] C. Zeng and V. Elser, Phys. Rev. B **42**, 8436 (1990).
[2] J. B. Marston and C. Zeng, J. Appl. Phys. **69**, 5962 (1991).
[3] M. B. Hastings, Phys. Rev. B **63**, 014413 (2000).
[4] P. Nikolic and T. Senthil, Phys. Rev. B **68**, 214415 (2003).
[5] R. R. P. Singh and D. A. Huse, Phys. Rev. B **76**, 180407 (2007).
[6] R. R. P. Singh and D. A. Huse, Phys. Rev. B **77**, 144415 (2008).
[7] Y. Iqbal, F. Becca, and D. Poilblanc, New J. Phys. **14**, 115031 (2012).
[8] V. Kalmeyer and R. B. Laughlin, Phys. Rev. B **39**, 11879 (1989).
[9] S. Sachdev, Phys. Rev. B **45**, 12377 (1992).
[10] K. Yang, L. K. Warman, and S. M. Girvin, Phys. Rev. Lett. **70**, 2641 (1993).
[11] G. Misguich, D. Serban, and V. Pasquier, Phys. Rev. Lett. **89**, 137202 (2002).
[12] F. Wang and A. Vishwanath, Phys. Rev. B **74**, 174423 (2006).
[13] S. Ryu, O. I. Motrunich, J. Alicea, and M. P. A. Fisher, Phys. Rev. B **75**, 184406 (2007).
[14] Y. Ran, M. Hermele, P. A. Lee, and X.-G. Wen, Phys. Rev. Lett. **98**, 117205 (2007).
[15] M. Hermele, Y. Ran, P. A. Lee, and X.-G. Wen, Phys. Rev. B **77**, 224413 (2008).
[16] H. C. Jiang, Z. Y. Weng, and D. N. Sheng, Phys. Rev. Lett. **101**, 117203 (2008).
[17] Y. Iqbal, F. Becca, and D. Poilblanc, Phys. Rev. B **84**, 020407 (2011).
[18] Y.-M. Lu, Y. Ran, and P. A. Lee, Phys. Rev. B **83**, 224413 (2011).
[19] Y. Huh, M. Punk, and S. Sachdev, Phys. Rev. B **84**, 094419 (2011).
[20] L. Messio, B. Bernu, and C. Lhuillier, Phys. Rev. Lett. **108**, 207204 (2012).
[21] Y.-C. He, D. N. Sheng, and Y. Chen, Phys. Rev. Lett. **112**, 137202 (2014).
[22] Y.-C. He, D. N. Sheng, and Y. Chen, Phys. Rev. B **89**, 075110 (2014).
[23] Shou-Shu Gong, Wei Zhu, and D. N. Sheng, Sci. Rep. **4**, 6317 (2014).
[24] W. Zhu, S. S. Gong, and D. N. Sheng, arXiv:1410.4883.
[25] B. Bauer, L. Cincio, B. P. Keller, M. Dolf, G. Vidal, S. Trebst, and A. W. W. Ludwig, Nat. Commun. **5**, 5137 (2014).
[26] S. R. White, Phys. Rev. Lett. **69**, 2863 (1992).
[27] U. Schollwöck, Rev. Mod. Phys. **77**, 259 (2005).
[28] U. Schollwöck, Ann. Phys. **326**, 96 (2011).
[29] S. Yan, D. A. Huse, and S. R. White, Science **332**, 1173 (2011).
[30] S. Depenbrock, I. P. McCulloch, and U. Schollwöck, Phys. Rev. Lett. **109**, 067201 (2012).
[31] H. C. Jiang, Z. Wang, and L. Balents, Nat. Phys. **8**, 902 (2012).

[32] M. Freedman, C. Nayak, K. Shtengel, K. Walker, and Z. Wang, Ann. Phys. **310**, 428 (2004).
[33] M. A. Levin and X.-G. Wen, Phys. Rev. B **71**, 045110 (2005).
[34] D. Poilblanc, N. Schuch, D. Perez-Garcia, and J. I. Cirac, Phys. Rev. B **86**, 014404 (2012).
[35] N. Schuch, D. Poilblanc, J. I. Cirac, and D. Perez-Garcia, Phys. Rev. B **86**, 115108 (2012).
[36] Y.-C. He and Y. Chen, Phys. Rev. Lett. **114**, 037201 (2015).
[37] Y. Qi, Z.-C. Gu, and H. Yao, arXiv:1406.6364.
[38] O. Buerschaper, S. C. Morampudi, and F. Pollmann, Phys. Rev. B **90**, 195148 (2014).
[39] M. Iqbal, D. Poilblanc, and N. Schuch, Phys. Rev. B **90**, 115129 (2014).
[40] M. P. Zaletel and A. Vishwanath, Phys. Rev. Lett. **114**, 077201 (2015).
[41] J. T. Chalker, P. C. W. Holdsworth, and E. F. Shender, Phys. Rev. Lett. **68**, 855 (1992).
[42] D. A. Huse and A. D. Rutenberg, Phys. Rev. B **45**, 7536 (1992).
[43] I. Ritchey, P. Chandra, and P. Coleman, Phys. Rev. B **47**, 15342 (1993).
[44] L. Messio, C. Lhuillier, and G. Misguich, Phys. Rev. B **83**, 184401 (2011).
[45] O. Cepas and A. Ralko, Phys. Rev. B **84**, 020413 (2011).
[46] M. Spenke and S. Guertler, Phys. Rev. B **86**, 054440 (2012).
[47] G.-W. Chern and R. Moessner, Phys. Rev. Lett. **110**, 077201 (2013).
[48] A. B. Harris, C. Kallin, and A. J. Berlinsky, Phys. Rev. B **45**, 2899 (1992).
[49] P. Lecheminant, B. Bernu, C. Lhuillier, L. Pierre, and P. Sindzingre, Phys. Rev. B **56**, 2521 (1997).
[50] R. Suttner, C. Platt, J. Reuther, and R. Thomale, Phys. Rev. B **89**, 020408 (2014).
[51] H. Li and F. D. M. Haldane, Phys. Rev. Lett. **101**, 010504 (2008).
[52] M. A. Metlitski and T. Grover, arXiv:1112.5166.
[53] V. Alba, M. Haque, and A. M. Läuchli, Phys. Rev. Lett. **110**, 260403 (2013).
[54] F. Kolley, S. Depenbrock, I. P. McCulloch, U. Schollwöck, and V. Alba, Phys. Rev. B **88**, 144426 (2013).
[55] A. W. Sandvik, AIP Conf. Proc. **1297**, 135 (2010).
[56] A. Pelissetto and E. Vicari, Phys. Rep. **368**, 549 (2002).
[57] A. W. Sandvik, Phys. Rev. B **85**, 134407 (2012).
[58] S.-S. Gong, W. Zhu, L. Balents, and D. N. Sheng, Phys. Rev. B **91**, 075112 (2015).
[59] Y. Iqbal, D. Poilblanc, and F. Becca, Phys. Rev. B **91**, 020402 (2015).